High Power Laser Science and Engineering, (2025), Vol. 13, e48, 12 pages.
doi:10.1017/hpl.2025.30

HIGH POWER LASER SCIENCE AND ENGINEERING

RESEARCH ARTICLE

Large-scale timing synchronization based on linear-optics timing detectors

Tong Wang[1], Mingzhe Li[1], Yi Zhang[1], Jie Yang[1], Yulin Shen[1], Ke Zhang[1], Dehui Pan[1], Jiahui Yao[1], Haoyang Sun[1], and Ming Xin[1,2]

[1]*School of Electrical and Information Engineering, Tianjin University, Tianjin, China*

[2]*Tianjin Key Laboratory of Brain-Inspired Intelligence Technology, Tianjin, China*

(Received 2 November 2024; revised 28 February 2025; accepted 2 April 2025)

Abstract

We presented an attosecond-precision timing detector based on linear optics. The minimum measurement floor is 1×10^{-10} fs^2/Hz with only 1 mW input optical power. With this novel technique, the residual dispersion of a 5.2 km fiber link is characterized and precisely compensated. Finally, a comprehensive feedback model has been developed to analyze the noise coupling in a long-distance link stabilization system. The simulation results demonstrate an out-of-loop jitter of merely 359 as, integrated at [1 Hz, 1 MHz], at 1 mW input power per photodetector of our timing detector. Remarkably, the system is capable of maintaining sub-femtosecond precision even at optical power levels as low as 240 nW (for a 5.2 km link length), or link lengths as long as 20 km (with 1 μW optical power), respectively.

Keywords: dispersion compensation; link stabilization; metrology; timing synchronization

1. Introduction

Precise timing synchronization is tremendously important in the large-scale scientific facilities[1]. For instance, in high-power laser facilities (HPLFs) such as the SG-II project[2] in China, the HERCULES laser[3,4], the SULF laser[5], the J-KAREN-P laser[6] and the Texas Petawatt Laser[7], coherent beam combining (CBC) is regarded as a promising approach to increase the extreme intensity[8–10]. The key to achieving high-efficiency CBC lies in ensuring that each individual laser is precisely spatially co-aligned and timing-synchronized with exceptional precision. To achieve even greater laser intensities, ultrahigh-power laser facilities, including Apollon[11], ELI-NP[12], EP-OPAL[13] and SEL[14], capable of delivering outputs of 10 PW and above, are currently being developed, in which timing synchronization plays an even more important role. In addition to HPLFs, the next-generation X-ray free electron lasers (XFELs) have also garnered significant global attention[15]; these include the European XFEL in Germany, FERMI[16] in Italy, SwissFEL in Switzerland and the Linac Coherent Light Source (LCLS)[17] along with LCLS II in the US[18]. To achieve the goal of generating attosecond (as, 10^{-18} s) X-ray pulses[19] of unparalleled brightness and filming ultrafast physical and chemical processes with the spatial-temporal resolution of atoms, attosecond-precision timing synchronization is exigently required.

A typical synchronization system comprises a timing reference that produces exceptionally stable timing signals, a target signal that requires alignment, a timing detector that assesses the timing difference between the target and reference signals and a control unit that adjusts the timing of the target to match the reference. When the target device is located far from the reference, a timing link is essential to convey the timing signal from the reference to the target[20].

The passively mode-locked laser (MLL), which shows ultra-low timing jitter at high frequencies (e.g., <1 fs above 10 kHz)[21], is considered as an ideal timing reference for synchronizing multiple microwave and optical sources. To break the limitation of amplitude modulation (AM)–phase modulation (PM) noise and provide precise timing resolution for the synchronization system, the balanced optical cross-correlator (BOC)[22,23] scheme was introduced. Over the past decades, the pulse-based BOC timing synchronization method has benefited several extreme laser facilities, such as SULF, ELI, the European XFEL, FERMI, SwissFEL and LCLS II.

However, as science facilities become steadily more complex, the limitations of the BOC timing synchronization

Correspondence to: M. Xin, School of Electrical and Information Engineering, Tianjin University, Tianjin 300072, China. Email: xinm@tju.edu.cn

system are gradually emerging. Currently, the primary challenge facing BOC-based timing synchronization systems lies in the inherent contradiction between optical power and synchronization precision. To ensure sub-fs synchronization precision while simultaneously suppressing additional timing jitter induced by fiber nonlinear effects[20], the optical power transmitted through the link must be constrained within the range of 10–20 mW. Taking transmission losses into account, this constraint limits the link length to under 5 km. In addition, since the output power of an MLL oscillator is usually 100–200 mW, the maximum number of synchronization terminals is also limited to approximately 10. Such limitations significantly impede the scalability of femtosecond-pulse-based timing synchronization technology toward greater distances and larger-scale implementations, thereby failing to meet the growing demands of large scientific facilities in terms of both physical dimensions and the number of terminal nodes.

To improve the scalability of these large facilities and ensure their continued operation with remarkable stability over the forthcoming decades, an ultra-precise timing and synchronization system that efficiently utilizes optical power and maintains a compact layout is urgently desired. In this paper, we have proposed a novel timing synchronization technology based on linear-optics timing detectors (LOTDs)[24]. Each timing link can be stabilized to sub-fs precision with less than 1 mW optical power; therefore, the additional timing jitter induced by fiber nonlinear effects can be neglected. This work would potentially extend synchronization distances from several kilometers to tens of kilometers, and enable a single MLL oscillator to synchronize hundreds of terminals rather than just a few, paving the way for more sophisticated and powerful scientific facilities.

In the following, a detailed theoretical and experimental demonstration of the LOTD is first given in Sections 2 and 3. Using this timing detector, the residual dispersion of a 5.2 km fiber link is precisely compensated in Section 4. A detailed feedback model is then built to analyze the factors influencing the out-of-loop timing jitter in Section 5. Finally, a simulation of the complete timing link stabilization system with our new timing method is presented, which can satisfy the critical and demanding synchronization needs of next-generation photon science facilities and will be experimentally carried out in our future work.

2. Working principle of the linear-optics timing detector

Figure 1(a) illustrates the basic principle of the LOTD. The input from the laser source is injected into an acousto-optic modulator (AOM), which diffracts the pulse trains into different directions. A radio-frequency (RF) signal is then applied to the AOM to generate the original zeroth-order light and the modulated first-order light. The timing target under measurement is placed in the path of the first-order light, introducing a perturbative timing error Δt to the optical signal. A 3 dB fiber coupler integrates the two diffracted light paths, generating beat note signals that are subsequently detected by a photodiode (PD).

For the input optical pulse train, we can describe its electric field by the following expression:

$$E_0(t) = \sum_{k=-\infty}^{+\infty} A\,(t - kT)\, e^{-j\omega_0 t}, \tag{1}$$

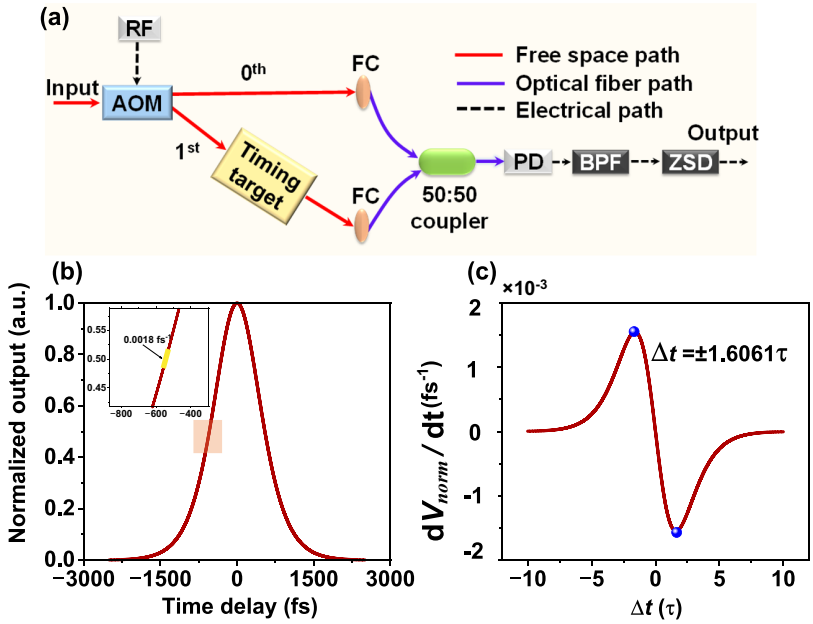

Figure 1. (a) Basic concept of the LOTD. FC, fiber collimator. (b) Simulated timing characterization curve, $\alpha = 1$, $\tau = 170$ fs. (c) Normalized timing sensitivity with different timing errors.

In Equation (1), $A(t)$ characterizes the temporal envelope function, ω_0 defines the optical carrier frequency and T represents the temporal separation between pulses. The optical fields entering the collimators from the zeroth- and first-order diffraction light can be expressed as follows:

$$E_0(t) = \sum_{k=-\infty}^{+\infty} A(t-kT)\, e^{-j\omega_0 t} = \sum_{n=-\infty}^{+\infty} A_n e^{-jn\omega_{\mathrm{rep}} t} e^{-j\omega_0 t}, \tag{2}$$

$$\begin{aligned} E_1(t) &= \sum_{k=-\infty}^{+\infty} A(t-\Delta t-kT)\, e^{-j(\omega_0+\omega_{\mathrm{RF}})(t-\Delta t)} \\ &= \sum_{n=-\infty}^{+\infty} B_n e^{-jn\omega_{\mathrm{rep}} t} e^{-j(\omega_0+\omega_{\mathrm{RF}})(t-\Delta t)}, \end{aligned} \tag{3}$$

where $f_{\mathrm{rep}} = 1/T$ is the pulse train repetition frequency, f_{RF} is the frequency of the RF driving signal, $\omega_{\mathrm{rep}} = 2\pi f_{\mathrm{rep}}$, $\omega_{\mathrm{RF}} = 2\pi f_{\mathrm{RF}}$ and A_n, B_n are the Fourier series of the zeroth- and first-order pulse train profiles. After passing through the coupler, the optical power reaching the PD is given by the following:

$$P(t,\Delta t) \propto \left|E_0 - jE_1\right|^2 = |E_0|^2 + |E_1|^2 + j\left(E_0 E_1^* - E_0^* E_1\right). \tag{4}$$

To filter out the ω_{RF} frequency component $P(t, \Delta t)$, we use a band pass filter (BPF). Thus, the output signal is given by the following:

$$\begin{aligned} V_{\mathrm{BPF}} \propto j \sum_{n=-\infty}^{+\infty} \Big[& A_n B_n^* e^{j\left[\omega_{\mathrm{RF}} t - (\omega_0+\omega_{\mathrm{RF}})\Delta t\right]} \\ & - A_n^* B_n e^{-j\left[\omega_{\mathrm{RF}} t - (\omega_0+\omega_{\mathrm{RF}})\Delta t\right]} \Big] \\ = X \cos & \left[\theta + \omega_{\mathrm{RF}} t - (\omega_0+\omega_{\mathrm{RF}})\Delta t\right], \end{aligned} \tag{5}$$

where $X = \left|\sum_{n=-\infty}^{+\infty} A_n B_n^*\right|$, and $j\sum_{n=-\infty}^{+\infty} A_n B_n^* = X e^{j\theta}$. It should be noted that the timing information Δt is reflected in both the amplitude and phase part of V_{BPF}. To eliminate the distraction of the phase component, a zero-bias Schottky diode (ZSD) is employed to extract the power fluctuation of V_{BPF}, thereby simplifying the resolution of Δt. Using the principle of Parseval's theorem, the ZSD response can be formulated as follows:

$$V_{\mathrm{ZSD}}(\Delta t) \propto \left|\sum_{n=-\infty}^{+\infty} A_n B_n^*\right|^{\alpha} \propto \left|\int_{-\infty}^{+\infty} A(t) A(t-\Delta t)\, \mathrm{d}t\right|^{\alpha}, \tag{6}$$

where α denotes a parameter linked to the nonlinear behavior of the ZSD. Hence, the timing characterization curve that indicates the relationship between timing error Δt and V_{ZSD} can be derived. Suppose $A(t)$ is a hyperbolic secant function[25]:

$$A(t) = A_0 \operatorname{sech}(t/\tau), \tag{7}$$

where τ is a parameter that characterizes the pulse width. Substituting Equation (7) into Equation (6), the analytical solution of V_{ZSD} can be further derived as follows:

$$V(\Delta t) \propto \begin{cases} \left(\frac{4\Delta t e^{\Delta t/\tau}}{e^{2\Delta t/\tau}-1}\right)^{\alpha}, & \Delta t \neq 0, \\ (2\tau)^{\alpha}, & \Delta t = 0. \end{cases} \tag{8}$$

To eliminate all the trivial coefficients, the normalized voltage can be used:

$$V_{\mathrm{norm}}(\Delta t) = \frac{V(\Delta t)}{V(0)} = \left(\frac{2\frac{\Delta t}{\tau} e^{\Delta t/\tau}}{e^{2\Delta t/\tau}-1}\right)^{\alpha}. \tag{9}$$

A simulated normalized timing curve is given in Figure 1(b). On either side of this curve, V_{norm} shows a consistent and monotonic change with Δt, which means it can be used to characterize Δt. In the magnified portion, the maximum slope of 0.0018 fs^{-1} is obtained, giving the maximum timing sensitivity. Based on Equation (9), the normalized timing sensitivity is given by the following:

$$\frac{\mathrm{d}V_{\mathrm{norm}}}{\mathrm{d}\Delta t} = \frac{1}{\tau} f(x), \tag{10}$$

where

$$x = \frac{\Delta t}{\tau}, \tag{11}$$

$$f(x) = 2\alpha\left(\frac{2xe^x}{e^{2x}-1}\right)^{\alpha-1} e^x \frac{e^{2x}(1-x)-(1+x)}{\left(e^{2x}-1\right)^2}. \tag{12}$$

Figure 1(c) shows the relationship between the normalized timing sensitivity and Δt. At the two peaks, the maximum sensitivity can be achieved when $\Delta t = \pm\, 1.6061\tau$.

The balanced detection is commonly employed to effectively lower the timing detection floor. A typical balanced operation consists of two identical timing detection circuits with a relative time delay, as shown in Figure 2(a). The zeroth-order light from the AOM is split into two paths, one of which incorporates a fixed delay T_{D}. Simultaneously, the first-order diffraction light is divided via a 50:50 coupler: one branch combines with the undelayed zeroth-order light, while the other combines with the T_{D}-delayed zeroth-order light through two additional 50:50 couplers. Both combined beams are processed through the PD, BPF and ZSD to generate independent timing signals. By differentially analyzing these two outputs, common-mode noises such as laser amplitude fluctuations and environmental disturbances are theoretically canceled, thereby enhancing the timing precision.

The balanced output voltage is given by the following:

$$V_{\mathrm{B}}(\Delta t) = V_{\mathrm{norm}}(\Delta t - T_{\mathrm{D}}) - V_{\mathrm{norm}}(\Delta t), \tag{13}$$

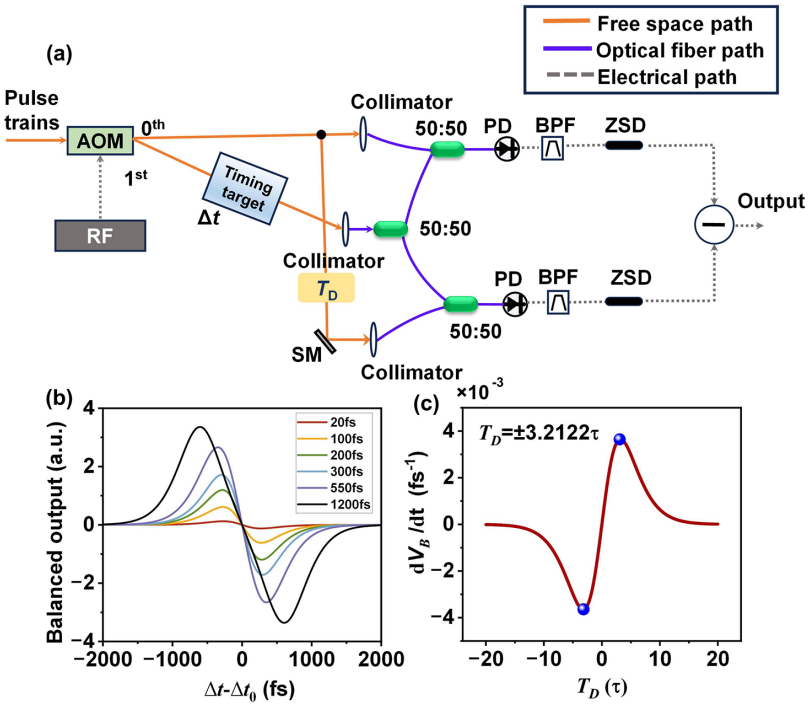

Figure 2. (a) Basic concept of the LOTD using balanced structure. (b) Balanced timing characterization curve with different delay T_D. (c) Balanced normalized timing sensitivity with different delay T_D.

and the corresponding timing curve becomes an 's' shape, as depicted in Figure 2(b). At the zero-crossing Δt_0 of this curve, $V_B(\Delta t_0) = 0$, that is, $V_{norm}(\Delta t_0 - T_D) = V_{norm}(\Delta t_0)$. Based on the symmetry of $V_{norm}(\Delta t)$, $\Delta t_0 = T_D/2$. In order to attain maximum timing sensitivity at the crossing point, the slope of $V_{norm}(\Delta t - T_D)$ and $V_{norm}(\Delta t)$ at $\Delta t = \Delta t_0$ needs to be maximum and minimum, respectively. Therefore, the optimum delay time for balanced detection is $T_D = \pm 3.2212 \cdot \tau$ the detailed relation between $dV_B/d\Delta t$ and T_D is given in Figure 2(c)). In Figure 2(b), several balanced timing curves with different T_D values are plotted; the one with T_D= 550 fs (closest to 3.2122τ) gives the maximum timing sensitivity around the zero-crossing point.

The LOTD has two key inherent advantages that make it well-suited for various applications. Firstly, if the zeroth- and first-order pulse trains have the same chirp, the dispersion phase coefficients can be canceled by the product $A_n B_n^*$ in Equation (6). Therefore, transform-limited pulse widths are not essential for maintaining high timing detection sensitivity. This characteristic is particularly beneficial in situations where it is difficult or cost-prohibitive to compensate for high-order dispersion, yet identical chirp between two pulse trains is readily achievable, as exemplified in ultra-long fiber loop-based timing sensors. In addition, it offers enhanced timing resolution at low power levels when compared to nonlinear-optics-based detectors such as the BOC. Taking advantage of this merit, it is possible to perform timing link stabilization with ultra-low optical power, which will be discussed in Section 5.

3. Balanced linear-optics timing detector experimental characteristics

The detailed experimental setup of the balanced linear-optics timing detector (BLOTD) is presented in Figure 3(a). A stable MLL source (MENHIR-1550) generates pulse trains centered at 1555 nm with 216.667 MHz repetition frequency and 170 fs duration, and subsequently injected into an AOM. An 80 MHz sinusoidal waveform from a function generator, initially at 200 mV root mean square (RMS), is amplified to 36 dBm to drive the AOM. The power distribution between the zeroth- and first-order paths of diffraction light should be near-equal.

A motorized delay line (MDL) is positioned in the first-order path to introduce a time delay Δt between the two beams. Balanced detection requires two independent timing measurement circuits for the zeroth- and first-order light. In the first circuit, the relative time delay between the two beams is Δt, while the second circuit introduces an additional delay T_D (total: $\Delta t + T_D$). To implement this, the zeroth-order light from the AOM is split into two paths via a polarization beam splitter (PBS). The light in one path is reflected by a silver mirror (SM) mounted on a manual stage, so as to pass twice through a quarter-wave plate. By finely adjusting the distance between the SM and the PBS using the manual stage, the relative delay T_D for the optimal timing sensitivity near the zero-crossing point of the 's'-shaped curve can be obtained. With the help of three 50:50 fiber couplers, the

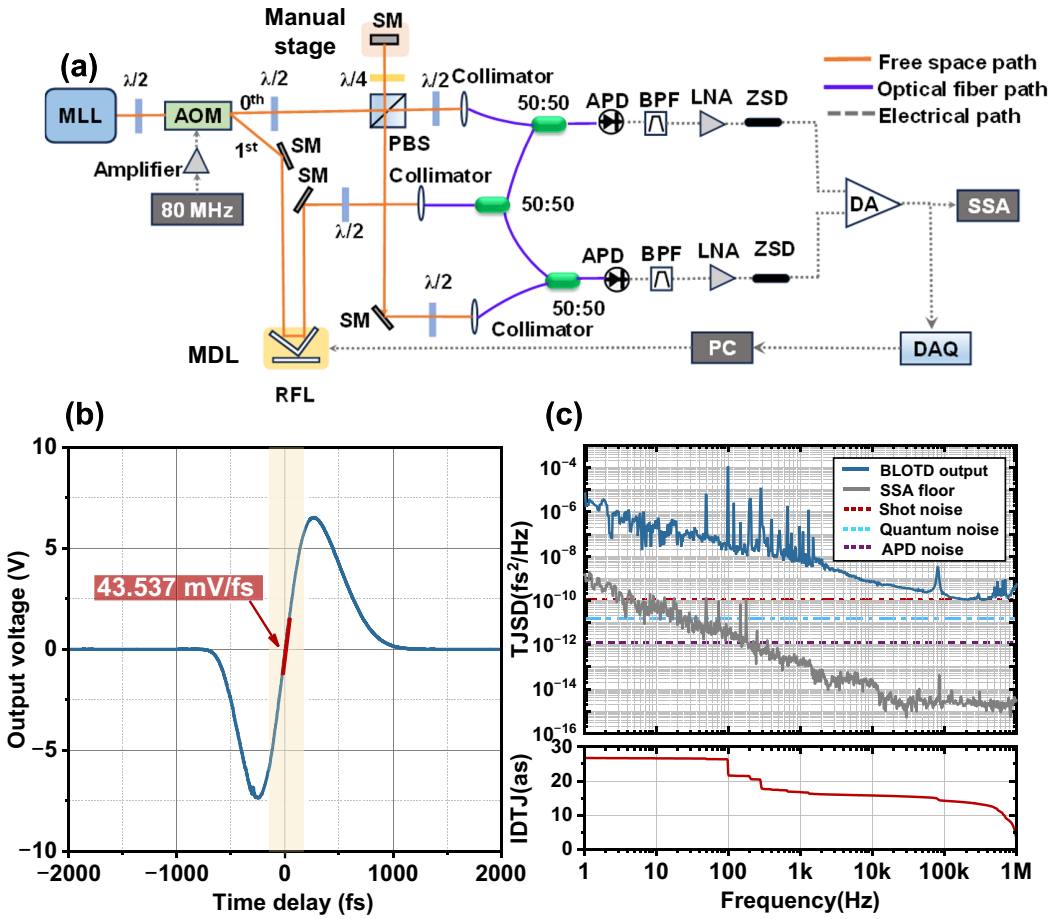

Figure 3. (a) The experimental setup for the BLOTD. λ/2, half-wave plate; λ/4, quarter-wave plate; PBS, polarization beam splitter; RFL, retroreflector; 50:50, 3 dB coupler; PC, personal computer; DA, differential amplifier. (b) Measured balanced timing characterization curve. (c) Measured results: TJSD and corresponding IDTJ.

zeroth- and first-order pulse trains beat on two avalanche photodiode detectors (APDs), and then two 80 MHz beat note signals can be obtained. The 100 MHz 3 dB bandwidth APD is customized with low noise equivalent power (2 pW/$\sqrt{\text{Hz}}$) and high responsivity (0.9 A/W). The beat note from each APD is initially extracted using a BPF and subsequently amplified by a low-noise amplifier (LNA). This process ensures that the power fluctuations, which contain the timing information of the beat note, are adequately amplified for further extraction by the ZSD. The balanced detection is finally achieved by differentially amplifying the two ZSDs' outputs. The differential amplifier is driven by a matched low-noise power supply. The timing characterization curve, which illustrates the relationship between Δt and the ZSD output, is generated by recording the output voltage through a data acquisition card (DAQ) while concurrently moving the computer-controlled MDL. With 1 mW power for each pulse train at each APD, the timing sensitivity around the zero-crossing is about 43.537 mV/fs, as shown in Figure 3(b). Due to the nonuniformity of the two ZSDs, the s-like curve in Figure 3(b) is a little asymmetric.

The timing jitter spectral density (TJSD) of the BLOTD is assessed by routing the output from the differential amplifier to the baseband port of a signal source analyzer (SSA). The findings are illustrated with the dark blue curve in Figure 3(c). The lowest measured timing detection noise floor reaches approximately 1×10^{-10} fs^2/Hz, which is nearly at the shot-noise limit (marked by the red dashed line). By opting for photodetectors with enhanced responsivity, it is feasible to further decrease the detection floor and approach the standard quantum limit for timing jitter in pulse trains, as predicted in Ref. [26] (represented by the blue dashed line), which is only 10 dB higher than the current detection threshold. Displayed at the bottom of Figure 3(c) is the integrated timing jitter (IDTJ). The total IDTJ within the range of 1 Hz to 1 MHz is found to be only 26.57 as.

4. Residual dispersion compensation with the linear-optics timing detector

In a typical pulse-based large-scale timing synchronization system[20], the timing link is stabilized by comparing the

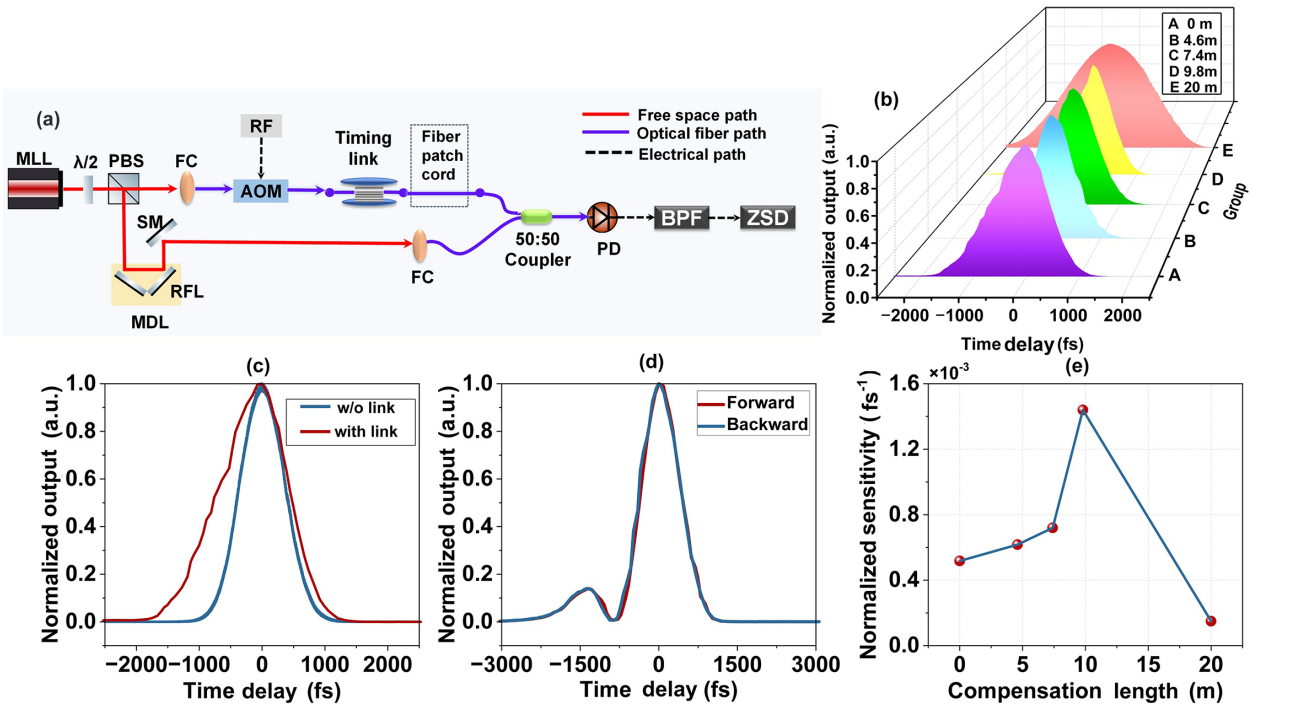

Figure 4. Experimental setup for residual dispersion compensation and results. (a) Experimental setups. (b) Timing curve with different fiber patch cord lengths. (c) Measured timing curves with and without the timing link. (d) Timing curve measured with MDL movements in the forward and backward directions. (e) Normalized timing sensitivity with different fiber patch cord lengths.

relative timing error between the round-trip link pulse and the new incoming pulse from the master laser. The dispersion of the timing link needs to be carefully compensated to guarantee high-precision timing detection as well as to restrict the Gordon–Haus timing jitter[27] generated during link transmission. In this section, with the help of the LOTD, the residual dispersion of a timing link can be easily measured, and then accurate dispersion compensation can be performed afterwards.

In Equation (6), if the zeroth- and first-order pulse trains do not have the same chirp, the dispersion phase coefficients can no longer be canceled by the product $A_n B_n^*$, which will broaden the timing curve. Therefore, the width of the timing curve can be used to characterize the link residual dispersion. The experimental setup is implemented as shown in Figure 4(a). The output of the MLL is separated into two paths. An AOM is placed in one path to shift the optical pulses' carrier frequency before they enter the timing link. The relative timing errors between the link pulse and the original laser pulse are measured by the LOTD electronics (PD, BPF and ZSD), and the timing curve can be obtained by moving the MDL. The timing link is composed of 4.5 km single-mode fiber (SMF) and 0.7 km dispersion compensating fiber (DCF). The DCF can compensate both the second- and third-order dispersion of the SMF simultaneously. To allow room for fine adjustments, the DCF overcompensates for the dispersion of about 10 m SMF.

The measured timing curves with and without the timing link are compared in Figure 4(c), in which an obvious broadening effect is observed due to the links' residual dispersion. Different lengths of fiber patch cord are then introduced to finely tune the residual dispersion. With 4.8 m fiber patch cord, the two measured timing curves by moving the MDL in the forward and backward directions are compared in Figure 4(d). The two curves exhibit near-perfect overlap, indicating that the temperature drift of the timing link does not affect the measurement results. The timing curves with different lengths of fiber patch cord are given in Figure 4(b), and the maximum normalized timing sensitivity for each case is summarized in Figure 4(e). With 9.8 m patch cord, the narrowest timing curve is obtained with the highest timing sensitivity, which means the residual dispersion of the timing link is almost compensated.

5. Feedback model of the balanced linear-optics timing detector-based timing link stabilization

After the timing link's dispersion is precisely compensated, it can be used to realize large-scale remote timing synchronization. Figure 5 gives a setup for timing link stabilization using the BLOTD. In the link stabilization block, the input optical pulse train is divided into two pulse trains in the reference path and in the link path. The link path consists of an MDL, an AOM, a fiber stretcher, a dispersion-compensated fiber link, a 45° Faraday rotator and a 40/60 transmission/reflection fiber mirror. The 45° Faraday rotator can make sure that the polarization directions of forward and

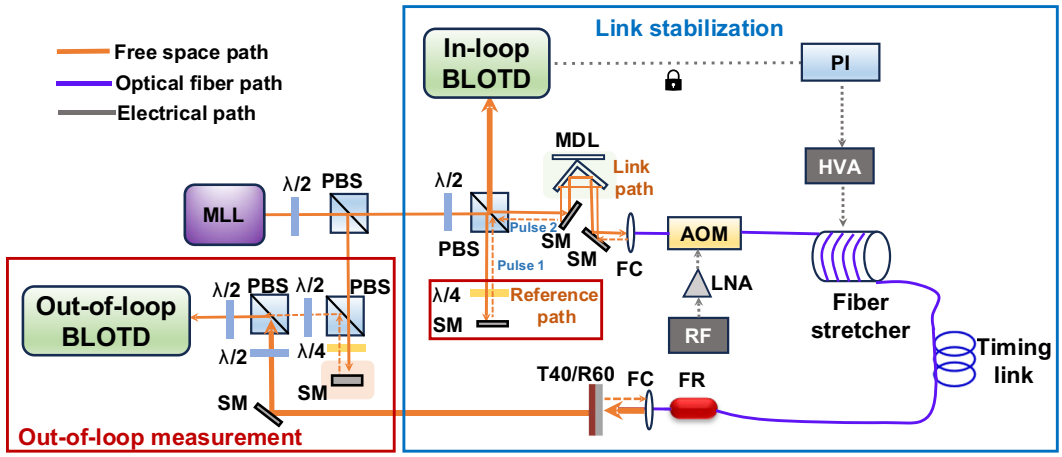

Figure 5. Detailed scheme of the link network stabilization. HVA, high-voltage amplifier; T40/R60, transmission 40%/reflection 60% fiber mirror; FR, Faraday rotator.

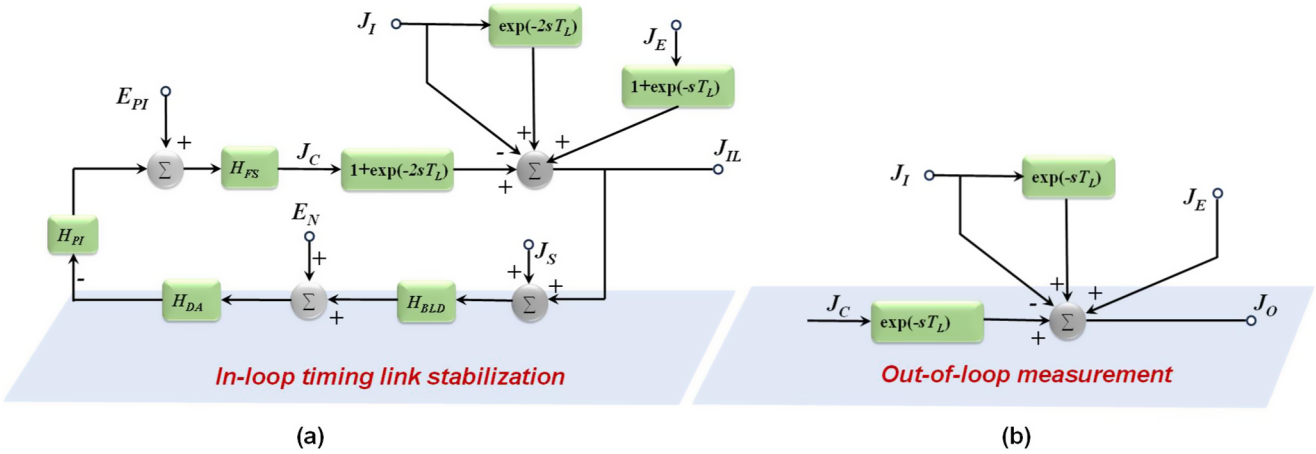

Figure 6. Feedback flow diagrams of (a) in-loop timing link stabilization and (b) out-of-loop jitter measurement. Here, ω is the complex frequency and $s = j\omega$; J_{I}, inherent jitter of the mode-locked laser; J_{E}, environmental jitter imposed on the link for single-trip link transmission; J_{IL}, detected timing jitter by the in-loop BLOTD; H_{BLD}, transfer function of the in-loop BLOTD; E_{N}, electronic noise in the in-loop BLOTD electronics; H_{DA}, transfer function of the differential amplifier in the BLOTD; H_{PI}, transfer function of the PI controller; E_{PI}, electronic noise of the PI controller; H_{FS}, transfer function of the fiber stretcher; J_{C}, equivalent timing delay generated by the control loop for compensation; J_{S}, shot-noise-equivalent timing jitter; T_{L}, single-trip link transmission time; J_{O}, relative timing jitter between the link output pulses and the original pulses from the mode-locked laser.

backward transmitted light in the link are orthogonal, so as to minimize the timing jitter induced by polarization mode dispersion. The relative timing error J_{IL} between the pulses in the reference and link path is measured by the in-loop BLOTD and fed back to control the fiber stretcher through a proportional–integral (PI) controller, and thus can stabilize the length of the timing link. In the out-of-loop measurement block, the residual timing jitter J_{O} between the link output pulse and the original pulse from the MLL is measured by the out-of-loop BLOTD to evaluate the performance of the link stabilization.

Since the BLOTD is a linear-optics device, it is possible to operate this link stabilization with very low power levels. To investigate the minimum required optical power for sub-fs precision link stabilization, based on the setup in Figure 5, a feedback model using experimental parameters is constructed. The flow diagram of the feedback model is shown in Figure 6.

The in-loop BLOTD detected timing jitter J_{IL} and the shot-noise-equivalent timing jitter J_{S} are converted to voltage signals with the BLOTD transfer function H_{BLD}, amplified by the differential amplifier H_{DA} together with the electronic noise $E_{\mathrm{N}}(\mathrm{V}/\sqrt{\mathrm{Hz}})$, and then sent to the PI controller H_{PI}. The output of the PI controller with additive noise E_{PI} then undergoes amplification and subsequent conversion to timing delays J_{C} through the fiber stretcher transfer function H_{FS}, where J_{C} acts as a compensating jitter to maintain the lock. Due to the round-trip link propagation, J_{C} is added to the link delay twice, and the round-trip link propagation time $2T_{\mathrm{L}}$ is accounted for in both J_{C} and the MLL's inherent jitter J_{I}; whereas single-trip link propagation time T_{L} is utilized for environmental jitter J_{E}, as the latter integrates all the single-trip environmental jitter in its definition. For the out-of-loop measurement, J_{C} and J_{I} experience a single-pass link propagation delay T_{L}. All the noise sources J_{I}, J_{E}, J_{S}, E_{N}, E_{PI} are characterized with the method in Appendix A. The

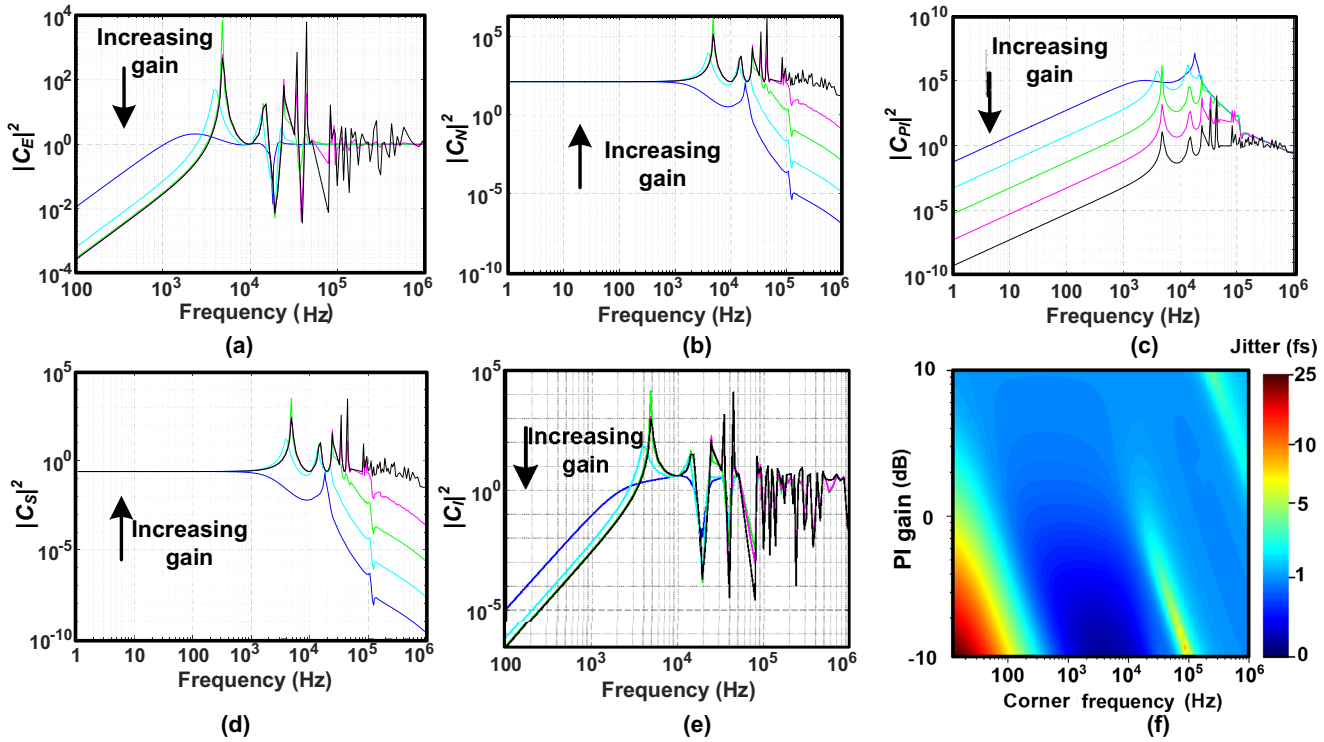

Figure 7. Simulation results for a 10.4 km timing link stabilization system. (a) The coefficient for the environmental noise imposed on the link. (b) The coefficient for the electronic noise. (c) The coefficient for the noise from the PI controller. (d) The coefficient for the shot noise. (e) The coefficient for the laser's inherent jitter. (f) Out-of-loop integrated timing jitter with different PI gains and corner frequencies (1 mW optical power at each PD of the in-loop BLOTD).

transfer functions can be calculated by the equations given in Appendix B.

Based on Figure 6, we have

$$J_{\mathrm{IL}} = J_{\mathrm{I}}\left[\exp\left(-2sT_{\mathrm{L}}\right)-1\right]+J_{\mathrm{E}}\left[\exp\left(-sT_{\mathrm{L}}\right)+1\right] + J_{\mathrm{C}}\left[\exp\left(-2sT_{\mathrm{L}}\right)+1\right], \tag{14}$$

$$J_{\mathrm{C}} = \left[-\left(J_{\mathrm{IL}}H_{\mathrm{BLD}}+J_{\mathrm{S}}H_{\mathrm{BLD}}+E_{\mathrm{N}}\right)H_{\mathrm{DA}}H_{\mathrm{PI}}+E_{\mathrm{PI}}\right]H_{\mathrm{FS}}, \tag{15}$$

$$J_{\mathrm{O}} = J_{\mathrm{I}}\left[\exp\left(-sT_{\mathrm{L}}\right)-1\right]+J_{\mathrm{E}}+J_{\mathrm{C}}\exp\left(-sT_{\mathrm{L}}\right). \tag{16}$$

Substituting Equations (14) and (15) into Equation (16), the explicit expression of J_{O} can be derived as follows:

$$J_{\mathrm{O}} = C_{\mathrm{I}}J_{\mathrm{I}}+C_{\mathrm{E}}J_{\mathrm{E}}+C_{\mathrm{S}}J_{\mathrm{S}}+C_{\mathrm{N}}E_{\mathrm{N}}+C_{\mathrm{PI}}E_{\mathrm{PI}}, \tag{17}$$

where

$$C_{\mathrm{I}} = \left[\exp\left(-sT_{\mathrm{L}}\right)-1\right]\frac{1+H\left[1-\exp\left(-sT_{\mathrm{L}}\right)\right]}{1+H\left[1+\exp\left(-2sT_{\mathrm{L}}\right)\right]}, \tag{18}$$

$$C_{\mathrm{E}} = \frac{1+H\left[1-\exp\left(-sT_{\mathrm{L}}\right)\right]}{1+H\left[1+\exp\left(-2sT_{\mathrm{L}}\right)\right]}, \tag{19}$$

$$C_{\mathrm{S}} = -\frac{H\exp\left(-sT_{\mathrm{L}}\right)}{1+H\left[1+\exp\left(-2sT_{\mathrm{L}}\right)\right]}, \tag{20}$$

$$C_{\mathrm{N}} = -\frac{H_{\mathrm{DA}}H_{\mathrm{PI}}H_{\mathrm{FS}}\exp\left(-sT_{\mathrm{L}}\right)}{1+H\left[1+\exp\left(-2sT_{\mathrm{L}}\right)\right]}, \tag{21}$$

$$C_{\mathrm{PI}} = \frac{H_{\mathrm{FS}}\exp\left(-sT_{\mathrm{L}}\right)}{1+H\left[1+\exp\left(-2sT_{\mathrm{L}}\right)\right]}, \tag{22}$$

$$H = H_{\mathrm{BLD}}H_{\mathrm{DA}}H_{\mathrm{PI}}H_{\mathrm{FS}}. \tag{23}$$

All the noise contributions C_iJ_i (i = E, S, I) and C_jE_j (j = N, PI) on the right-hand side of Equation (17) are mutually uncorrelated, and the mean values of their cross-products are cancelled. Consequently, the average out-of-loop jitter spectral density (s^2/Hz) can be represented as follows:

$$J_{\mathrm{O2}} = |C_{\mathrm{I}}|^2\overline{J_{\mathrm{I}}^2}+|C_{\mathrm{E}}|^2\overline{J_{\mathrm{E}}^2}+|C_{\mathrm{S}}|^2\overline{J_{\mathrm{S}}^2}+|C_{\mathrm{N}}|^2\overline{E_{\mathrm{N}}^2}+|C_{\mathrm{PI}}|^2\overline{E_{\mathrm{PI}}^2} \tag{24}$$

As Equation (24) indicates, J_{O} has five main contributions: the environmental noise imposed on the link; the electronic noise of the BLOTD; the noise introduced by the PI controller; the shot noise; and the inherent jitter of the MLL, with coefficients C_{E}, C_{N}, C_{PI}, C_{S} and C_{I}, respectively. Figures 7(a)–7(e) present the calculated coefficients $|C_i|$ (i = E, N, PI, S, I) with a 10.4 km link length for several distinct PI controller gain settings. To effectively reduce environmental noise and the laser's inherent noise at frequencies lower than 5 kHz, it is essential to maintain high gain settings, as demonstrated in Figures 7(a) and 7(e). Nevertheless, elevating the gain leads to increased BLOTD electronic noise and shot noise, as illustrated in

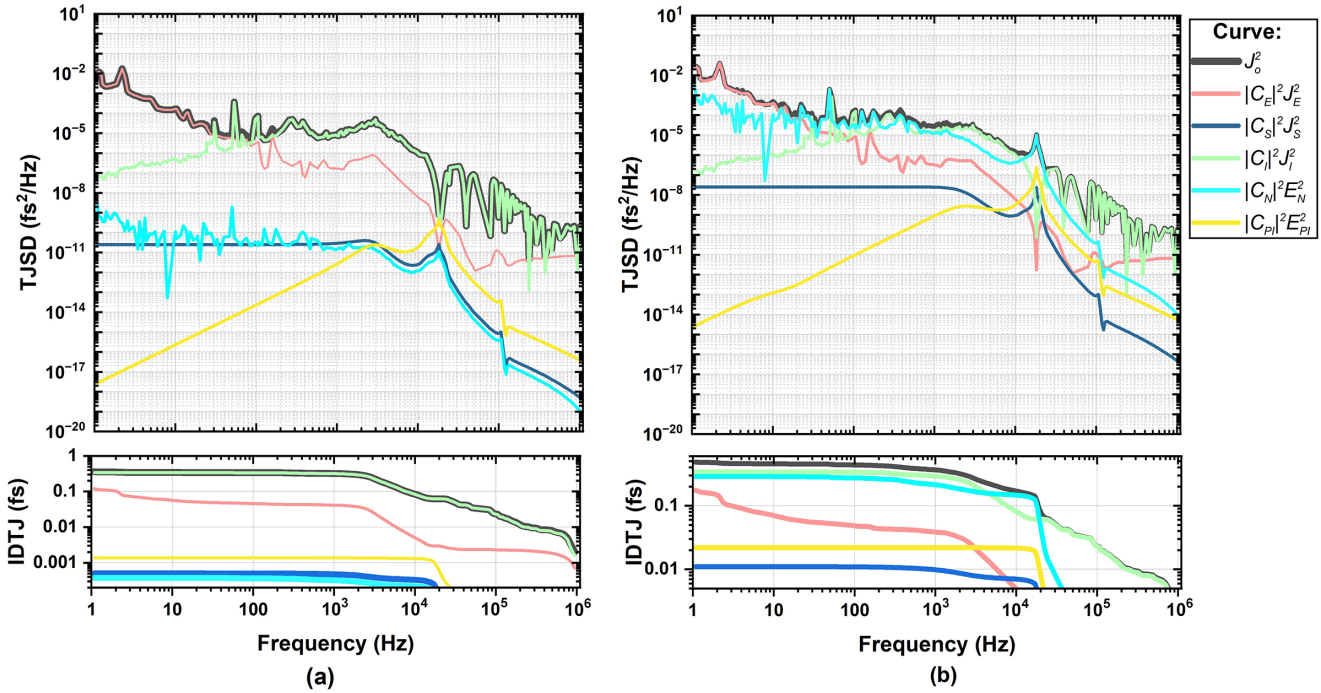

Figure 8. Out-of-loop jitter simulation results of individual jitter contributions with the optical power of (a) 1 mW and (b) 1 μW at each PD of the in-loop BLOTD. The timing link length is 10.4 km. The legend on the right shows the color code of the jitter spectral densities. Integrated jitter in this graph is shown on a logarithmic scale.

Figures 7(b) and 7(d). The large gain peaks can be observed near frequencies $n/4T_L$ ($n = 1, 3, 5, \ldots$) as well as the fiber stretcher's resonant frequency (approximately 18 kHz) in Figures 7(a)–7(e).

Using the calculated coefficients above, each noise contribution in Equation (24), as well as $J_O{}^2$, can be calculated. Typical experimental parameters are used in the simulation as given in Table 1 in Appendix C. Firstly, the optical power at each PD of the in-loop BLOTD is set as 1 mW. Through continuous optimization of the PI gain and corner frequency, we can achieve optimal link stabilization with minimal IDTJ of $J_O{}^2$, as shown in Figure 7(f). With the optimized PI controller settings, the TJSD of $J_O{}^2$ and each noise contribution are given in Figure 8(a). The total IDTJ from 1 Hz to 1 MHz is only 0.36 fs (black curve). The environmental jitter of the link (pink curve) is the predominant noise factor in the low-frequency range. The inherent noise contribution of the MLL becomes more noticeable for offset frequencies above 100 Hz.

To investigate the link stabilization performance at ultra-low power levels, the optical power at each PD of the in-loop BLOTD is reduced to 1 μW. After re-optimizing the PI controller parameters, the TJSD and IDTJ results are as shown in Figure 8(b), and the timing link can still maintain sub-fs precision with 0.48 fs IDTJ at [1 Hz, 1 MHz]. To compensate the low timing sensitivity of the BLOTD at the 1 μW power level, a larger feedback gain is necessary to help suppress the environmental noise of the timing link. Compared with Figures 8(a) and 8(b), it can be seen that as the link operational power decreases, both the shot noise and the electronic noise from the PI controller are elevated, while the electronic noise of the BLOTD increases the most dramatically and becomes the major contributor to the increase of IDTJ. Nevertheless, the total out-of-loop timing jitter is still dominated by J_E and J_I.

Furthermore, timing link stabilization with different fiber lengths is also simulated. Keeping the in-loop PD power as 1 μW, an IDTJ of 0.79 fs can still be achieved for 20 km link stabilization (Figure 9(a)). While if the link length is reduced to 5.2 km, an unprecedented low optical power of 240 nW at each in-loop PD is sufficient to provide sub-fs link stabilization precision (with 0.93 fs integrated jitter, as shown in Figure 9(b)). Leveraging the advantages of the BLOTD, we theoretically demonstrated the capability to extend the link length to nearly five times that of previous works using the BOC, and the required operational power is also reduced by more than three orders of magnitude. This breakthrough overcomes the current power-imposed limitations on transmission distance and the number of synchronization terminals, holding significant implications for the expansion and construction of various large-scale laser facilities.

6. Conclusions

In summary, we have experimentally demonstrated an attosecond-precision balanced linear-optics-based timing

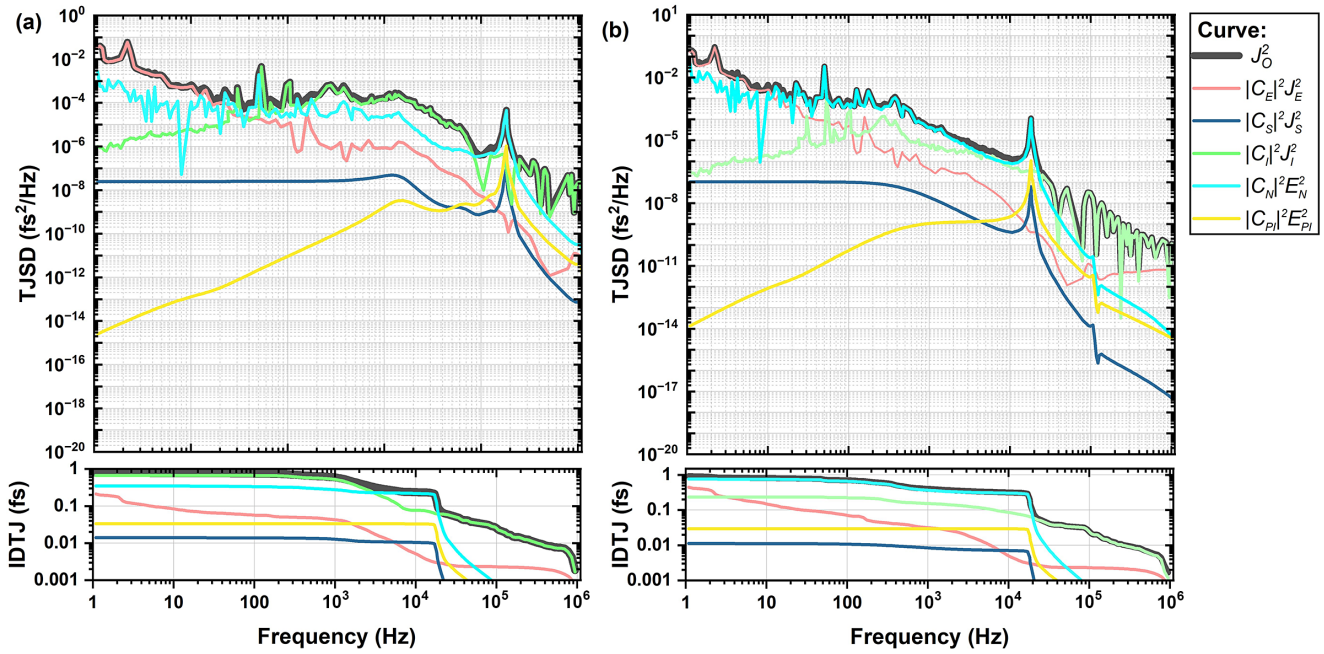

Figure 9. Out-of-loop jitter simulation results of individual jitter contributions at the in-loop PD power of (a) 1 μW with transmission length of 20 km and (b) 240 nW with transmission length of 5.2 km.

detector. With 1 mW power per pulse train per photodetector, a shot-noise-limited timing detection floor of 1×10^{-10} fs^2/Hz is achieved. The balanced configuration effectively mitigates environmental and laser amplitude noise. The total integrated jitter from 1 Hz to 1 MHz is merely 26.57 as. As one of the applications, we have conducted the residual dispersion evaluation with this powerful tool. Finally, we have presented a comprehensive jitter analysis for the timing link stabilization. At 1 mW and 1 μW optical power at each PD of the in-loop BLOTD, the 10.4 km link is stabilized with total integrated jitter of 0.359 fs and 0.48 fs, respectively. The system can still maintain sub-fs precision with lower optical power or longer link length. For instance, with 5.2 km link length, an integrated jitter of 0.93 fs can be achieved with only 240 nW power, while with 1 μW power, after 20 km link transmission, the residual timing jitter is only 0.79 fs.

We believe that the timing link stabilization at ultra-low optical power levels will not only greatly expand the distance and number of terminals of the current synchronization systems, but also be beneficial in many other cutting-edge fields such as ultra-long-range laser radar and gravitational wave detection.

Appendix

A. Noise source characterization

The inherent jitter J_I is obtained from our previous BOC characterization results of a commercial MLL[28]. The shot-noise-equivalent timing jitter J_S can be calculated by the Equation (9) of Ref. [24]. The electronic noise E_N of the BLOTD (generated from the photodetector, the BPF, the RF amplifiers, the ZSD and the differential amplifier) is measured when there is no input light in the system and then converted to timing jitter (in units of s/$\sqrt{}$Hz) by multiplying with the timing sensitivity. The environmental noise jitter J_E is divided into two parts: at low frequencies (<100 Hz), the noise is modeled by a combination of $1/f$ and $1/f^2$ noise, reflecting the typical properties of environmental noise; for frequencies of more than 100 Hz, the measured data from Ref. [29] are utilized. The electronic noise of the PI controller E_{PI} is evaluated utilizing a noise model predicated with the characteristics of the amplifier circuits presented in Figure 10(a), and can be estimated by Equations (25) and (26)[29]:

$$E_{PI}^2 = \frac{4Z_f^2 k_B T}{R_{in}} + 4k_B T R_f + \left(1+\frac{Z_f}{R_{in}}\right)^2 V_n^2, \tag{25}$$

$$Z_f = \frac{1/R_f - j\omega C}{(1/R_f)^2 + \omega^2 C^2}. \tag{26}$$

B. Transfer function calculation

The transfer functions H_{BLD}, H_{DA}, H_{PI} and H_{FS} in Figure 6 can be obtained by the following equations:

$$H_{BLD} = k_{BLD}, \tag{27}$$

$$H_{PI} = k_{PI}\left(\frac{s+2\pi f_{PI}}{s}\right), \tag{28}$$

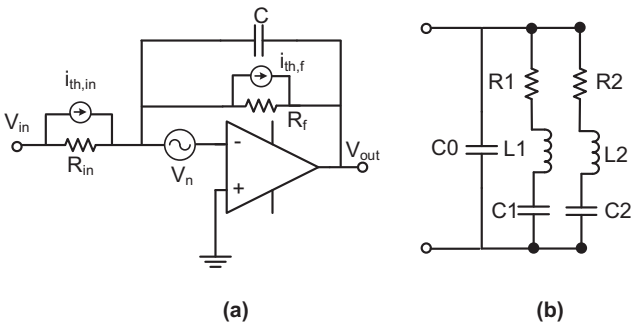

Figure 10. (a) Noise model of the PI controller. V_{in} and V_{out}, input and output voltage; V_n, input voltage noise of the PI controller; R_{in} and $i_{th,in}$, input impedance and its thermal noise current; R_f and $i_{th,f}$, feedback gain resistance and its thermal noise current; C, integrating capacitance. (b) Equivalent circuit of the fiber stretcher.

$$H_{DA} = \left(1 + \frac{s}{2\pi f_{BW}}\right)^{-1}, \tag{29}$$

$$H_{FS} = H_{PZT} H_F. \tag{30}$$

where k_{BLD} is the sensitivity of the BLOTD (in units of mV/fs), k_{PI} is the PI gain, f_{PI} is the PI corner frequency and f_{BW} is the 3 dB bandwidth of the differential amplifier. The transfer function H_{FS} is the product of two parts: the lead zirconate titanate (PZT) response function H_{PZT} fitted from manufacturer data and the filter function H_F by the equivalent driven circuits (shown in Figure 10(b))[30].

C. Typical parameters of the link stabilization used for simulation

Table 1. Parameters used for simulation of the timing link stabilization.

Parameter	Value	Unit
k_{BLD}	43.57 (with 1 mW input power)	mV/fs
f_{rep}	216.667	MHz
f_{BW}	1	MHz
R_{in}	1	MΩ
R_f	$k_{PI} \times R_{in}$	MΩ
C	10	nF
V_n	10^{-9}	V/$\sqrt{\text{Hz}}$
C_0	33	nF
C_1	5	nF
C_2	7	nF
R_1	26	Ω
R_2	3.2	Ω
L_1	15	mH
L_2	0.3	mH
T	300	K

Acknowledgements

This work was supported by the National Key R&D Program of China (Grant No. 2021YFC2201902) and the National Natural Science Foundation of China (Grant No. 61975149).

References

1. M. Xin, K. Şafak, and F. X. Kärtner, Optica, **5**, 1564 (2018).
2. Z. Lin, X. Deng, D. Fan, S. Wang, S. Chen, J. Zhu, L. Qian, X. Shen, F. Xu, J. Zhu, W. Ma, X. Xie, Y. Zheng, W. Zhang, Q. Chen, M. Ling, H. Huang, and J. Zhang, Fusion Eng. Des. **44**, 61 (1999).
3. S.-W. Bahk, P. Rousseau, T. A. Planchon, V. Chvykov, G. Kalintchenko, A. Maksimchuk, G. A. Mourou, and V. Yanovsky, Opt. Lett. **29**, 2837 (2004).
4. V. Yanovsky, V. Chvykov, G. Kalinchenko, P. Rousseau, T. Planchon, T. Matsuoka, A. Maksimchuk, J. Nees, G. Cheriaux, G. Mourou, and K. Krushelnick, Opt. Express **16**, 2109 (2008).
5. Z. Zhang, F. Wu, J. Hu, X. Yang, J. Gui, P. Ji, X. Liu, C. Wang, Y. Liu, X. Lu, Y. Xu, Y. Leng, R. Li, and Z. Xu, High Power Laser Sci. Eng. **8**, e4 (2020).
6. A. S. Pirozhkov, Y. Fukuda, M. Nishiuchi, H. Kiriyama, A. Sagisaka, K. Ogura, M. Mori, M. Kishimoto, H. Sakaki, N. P. Dover, K. Kondo, N. Nakanii, K. Huang, M. Kanasaki, K. Kondo, and M. Kando, Opt. Express **25**, 20486 (2017).
7. G. Tiwari, E. Gaul, M. Martinez, G. Dyer, J. Gordon, M. Spinks, T. Toncian, B. Bowers, X. Jiao, R. Kupfer, L. Lisi, E. McCary, R. Roycroft, A. Yandow, G. D. Glenn, M. Donovan, T. Ditmire, and B. M. Hegelich, Opt. Lett. **44**, 2764 (2019).
8. K. L. Baker, D. Homoelle, E. Utterback, and S. M. Jones, Opt. Express **17**, 19551 (2009).
9. J.-P. Chambaret, O. Chekhlov, G. Chériaux, J. Collier, R. Dabu, P. Dombi, A. M. Dunne, K. Ertel, P. Georges, J. Hebling, J. Hein, C. Hernandez-Gomez, C. Hooker, S. Karsch, G. Korn, F. Krausz, C. L. Blanc, Z. Major, F. Mathieu, T. Metzger, G. Mourou, P. Nickles, K. Osvay, B. Rus, W. Sandner, G. Szabó, D. Ursescu, and K. Varjú, Proc. SPIE **7721**, 77211D (2010),
10. A. V. Bashinov, A. A. Gonoskov, A. V. Kim, G. Mourou, and A. M. Sergeev, Eur. Phys. J. Spec. Top. **223**, 1105 (2014).
11. J. P. Zou, C. Le Blanc, D. N. Papadopoulos, G. Chériaux, P. Georges, G. Mennerat, F. Druon, L. Lecherbourg, A. Pellegrina, P. Ramirez, F. Giambruno, A. Fréneaux, F. Leconte, D. Badarau, J. M. Boudenne, D. Fournet, T. Valloton, J. L. Paillard, J. L. Veray, M. Pina, P. Monot, J. P. Chambaret, P. Martin, F. Mathieu, P. Audebert, and F. Amiranoff, High Power Laser Sci. Eng. **3**, e2 (2015).
12. S. Gales, K. A. Tanaka, D. L. Balabanski, F. Negoita, D. Stutman, O. Tesileanu, C. A. Ur, D. Ursescu, I. Andrei, S. Ataman, M. O. Cernaianu, L. D'Alessi, I. Dancus, B. Diaconescu, N. Djourelov, D. Filipescu, P. Ghenuche, D. G. Ghita, C. Matei, K. Seto, M. Zeng, and N. V. Zamfir, Rep. Prog. Phys. **81**, 094301 (2018).
13. J. Bromage, S.-W. Bahk, I. A. Begishev, C. Dorrer, M. J. Guardalben, B. N. Hoffman, J. B. Oliver, R. G. Roides, E. M. Schiesser, M. J. ShoupIII, M. Spilatro, B. Webb, D. Weiner, and J. D. Zuegel, High Power Laser Sci. Eng. **7**, e4 (2019).
14. X. Wang, X. Liu, X. Lu, J. Chen, Y. Long, W. Li, H. Chen, X. Chen, P. Bai, Y. Li, Y. Peng, Y. Liu, F. Wu, C. Wang, Z. Li, Y. Xu, X. Liang, Y. Leng, and R. Li, Ultrafast Sci. **2022**, 9894358 (2022).
15. R. Abela, A. Aghababyan, M. Altarelli, and C. Altucci, "XFEL: the European X-ray free-electron laser - technical design report", Technical Report (DESY XFEL Project Group, 2006).
16. E. Allaria, R. Appio, L. Badano, W. A. Barletta, S. Bassanese, S. G. Biedron, A. Borga, E. Busetto, D. Castronovo, P. Cinquegrana, S. Cleva, D. Cocco, M. Cornacchia, P. Craievich, I. Cudin, G. D'Auria, M. Dal Forno, M. B. Danailov, R. De Monte, G. De Ninno, P. Delgiusto, A. Demidovich, S. Di Mitri,

B. Diviacco, A. Fabris, R. Fabris, W. Fawley, M. Ferianis, E. Ferrari, S. Ferry, L. Froehlich, P. Furlan, G. Gaio, F. Gelmetti, L. Giannessi, M. Giannini, R. Gobessi, R. Ivanov, E. Karantzoulis, M. Lonza, A. Lutman, B. Mahieu, M. Milloch, S. V. Milton, M. Musardo, I. Nikolov, S. Noe, F. Parmigiani, G. Penco, M. Petronio, L. Pivetta, M. Predonzani, F. Rossi, L. Rumiz, A. Salom, C. Scafuri, C. Serpico, P. Sigalotti, S. Spampinati, C. Spezzani, M. Svandrlik, C. Svetina, S. Tazzari, M. Trovo, R. Umer, A. Vascotto, M. Veronese, R. Visintini, M. Zaccaria, D. Zangrando, and M. Zangrando, Nat. Photonics **6**, 699 (2012).

17. P. Emma, R. Akre, J. Arthur, R. Bionta, C. Bostedt, J. Bozek, A. Brachmann, P. Bucksbaum, R. Coffee, F.-J. Decker, Y. Ding, D. Dowell, S. Edstrom, A. Fisher, J. Frisch, S. Gilevich, J. Hastings, G. Hays, P. Hering, Z. Huang, R. Iverson, H. Loos, M. Messerschmidt, A. Miahnahri, S. Moeller, H.-D. Nuhn, G. Pile, D. Ratner, J. Rzepiela, D. Schultz, T. Smith, P. Stefan, H. Tompkins, J. Turner, J. Welch, W. White, J. Wu, G. Yocky, and J. Galayda, Nat. Photonics **4**, 641 (2010).
18. J. Stohr, "Linac Coherent Light Source II (LCLS-II) Conceptual Design Report", Technical Report (SLAC National Accelerator Laboratory, 2011).
19. E. Prat and S. Reiche, Phys. Rev. Lett. **114**, 244801 (2015).
20. M. Xin, K. Şafak, M. Y. Peng, A. Kalaydzhyan, W.-T. Wang, O. D. Mücke, and F. X. Kärtner, Light Sci. Appl. **6**, e16187 (2016).
21. H. A. Haus and A. Mecozzi, IEEE J. Quantum Electron. **29**, 983 (1993).
22. L. A. Jiang, S. T. Wong, M. E. Grein, E. P. Ippen, and H. A. Haus, IEEE J. Quantum Electron. **38**, 1047 (2002).
23. T. R. Schibli, J. Kim, O. Kuzucu, J. T. Gopinath, S. N. Tandon, G. S. Petrich, L. A. Kolodziejski, J. G. Fujimoto, E. P. Ippen, and F. X. Kärtner, Opt. Lett. **28**, 947 (2003).
24. T. Wang, Q. Ren, K. Şafak, F. X. Kärtner, and M. Xin, Opt. Express **29**, 38140 (2023).
25. H. A. Haus, IEEE J. Select. Top. Quantum Electron. **6**, 1173 (2000).
26. V. Giovannetti, S. Lloyd, and L. Maccone, Nature **412**, 417 (2001).
27. J. P. Gordon and H. A. Haus, Opt. Lett. **11**, 665 (1986).
28. K. Şafak, M. Xin, P. T. Callahan, M. Y. Peng, and F. X. Kärtner, Struct. Dyn. **2**, 041715 (2015).
29. K. Şafak, M. Xin, Q. Zhang, S.-H. Chia, O. D. Mücke, and F. X. Kärtner, Opt. Express **24**, 21752 (2016).
30. https://www.optiphase2.com/.